PHYSICAL REVIEW E **96**, 022222 (2017)

Lagrangian descriptors of driven chemical reaction manifolds

Galen T. Craven
Department of Chemistry, University of Pennsylvania, Philadelphia, Pennsylvania 19104, USA

Andrej Junginger
Institut für Theoretische Physik 1, Universität Stuttgart, 70550 Stuttgart, Germany

Rigoberto Hernandez[*]
Department of Chemistry, Johns Hopkins University, Baltimore, Maryland 21218, USA

(Received 6 April 2017; published 31 August 2017)

The persistence of a transition state structure in systems driven by time-dependent environments allows the application of modern reaction rate theories to solution-phase and nonequilibrium chemical reactions. However, identifying this structure is problematic in driven systems and has been limited by theories built on series expansion about a saddle point. Recently, it has been shown that to obtain formally exact rates for reactions in thermal environments, a transition state *trajectory* must be constructed. Here, using optimized Lagrangian descriptors [G. T. Craven and R. Hernandez, Phys. Rev. Lett. **115**, 148301 (2015)], we obtain this so-called distinguished trajectory and the associated moving reaction manifolds on model energy surfaces subject to various driving and dissipative conditions. In particular, we demonstrate that this is exact for harmonic barriers in one dimension and this verification gives impetus to the application of Lagrangian descriptor-based methods in diverse classes of chemical reactions. The development of these objects is paramount in the theory of reaction dynamics as the transition state structure and its underlying network of manifolds directly dictate reactivity and selectivity.

DOI: 10.1103/PhysRevE.96.022222

I. INTRODUCTION

A grand challenge in the modern study of reaction dynamics is the development of reaction rate theories to treat complex systems subjected to nonequilibrium forcing [1,2]. These systems occur across diverse fields, from materials science [3–5] to biology [6–9], and drive a broad range of emergent phenomena, such as field-induced locomotion [10] and assembly mechanisms [11–14]. In these driven environments, a suitable description of transition state [15] and post-transition state [16] structure must be developed to describe the respective reaction mechanism. Furthermore, in many systems the complexity of describing state transitions has required modification of the canonical view of the mechanisms that drive reactions from one state to another [17–19]. Thus, further theoretical characterization is needed in order to describe the microscopic mechanisms that give rise to observable macroscopic dynamical properties, such as reaction rates.

In the formulation of theory for chemical reactions that occur in simple and isolated environments, transition state theory (TST) is ubiquitous [17,20–28]. The allure of TST is its simplicity, as it allows the prediction of rates with only knowledge of the landscape of the underlying potential energy surface. The implementation of TST requires the construction of a dividing surface (DS) separating reactants and products [27,29] and, subsequently, a measure of the reactive flux through that DS. In conservative Hamiltonian systems, normally hyperbolic invariant manifolds (NHIM) [15,30,31] provide methods for the development of optimal DSs and the analysis of reaction geometries [19,32–36] at energies close to the reaction threshold [37–40]. However, on nonlinear energy surfaces, an analytical evaluation of the reactive flux integral is intractable (except in a few select cases), and the flux is measured directly using computational inefficient integration of large numbers of trajectories. In complex environments, deviations from TST arise as fluctuations in the environment may cause reactive trajectories to recross the DS many times. These recrossings contribute to an overestimate in the flux calculation, therefore TST gives an upper bound to the rate.

In reactions that are induced by external sources, time-dependent TST [25] has provided a framework to compute reaction rates through location of moving saddle points (time-dependent TSs) that provide anchors for reactive flux calculations. The hyperbolic trajectories [41–44] and associated manifolds that partition phase space into reactive and nonreactive portions have been termed transition state *trajectories* because they play the same role in describing nonautonomous dynamics as traditional TSs play in autonomous systems. Manipulation of these moving TSs through tailored pulses allows guiding reactions toward a desired product and furthermore toward the realization of optimal control of state transitions [45–50].

Nonstatistical effects in the reactive flux [51–56] can be prominent, specifically at the onset (transient) portions of the transition processes [57,58]. Moreover, describing the complex and often nonintuitive TS structures [19] in thermally activated [41–43] and field-induced reactions [57–60] has provided a significant hurdle to rate theory. Generalizations of normal form theory and other methodologies [47,61–66] built on the identification of reaction conduits that channel reactive trajectories into product states have given insight into the nature of phase-space structures dictating reactive events in complex environments. Recently, Lagrangian descriptors (LD) were introduced by Mancho and coworkers [67,68], motivated

---

[*] r.hernandez@jhu.edu

by the observation that positive bounded observables measured along single trajectories will have distinct and differing properties on each side of a phase space boundary. Methods built on LDs have provided insight into the nonautonomous dynamics in systems over a broad range of length scales from ocean flow patterns [67] to chemical reactions [69–71].

Here we provide a firmer foundation to the Lagrangian descriptor-based method developed in Ref. [69] by constructing the reaction geometry (RG) in both paradigmatic linear and nonlinear reactive systems subjected to various driving and dissipative conditions. This LD-RG method has also been shown to resolve the reaction dynamics of driven barrierless reactions [70] and one- and two- dimensional models of field-induced ketene isomerization [71]. The LD-RG method is first verified through application to a parabolic (harmonic) system in which the pertinent constructs can be obtained exactly. Application to an Eckart barrier is used to illustrate the extension of the LD-RG method to nonlinear systems. Through variation in geometry of the reaction pathway, we show that the physical insight gained from LD-RG is highly dependent on the shape of the potential energy surface and the underlying driving environment. Thermal activation is introduced in the reactive models in the mean-field sense through Langevin dynamics. In all reacting systems addressed thus far, the dividing surface associated with the TS trajectory constructed using LD-RG has been seen to be free of recrossings. Thus, this work is a significant advance beyond Refs. [69–71] because we now rigorously demonstrate that the LD-RG method can be used to construct a global non-recrossing transition state in the harmonic limit, and that it provides the structure of the manifolds associated with the transition state trajectory in linear and nonlinear systems under diverse environmental conditions. A principal implication of the results presented here is that reactive flux can be determined exactly in chemical reactions that occur in driven complex environments.

II. THEORY AND MODEL DETAILS

For reactions that occur in a condensed phase, thermal forces arise from solvent-reactant interactions. In the resulting thermal environment, or when the reaction is driven under dynamical load, the reactant to product conversion $\mathrm{R} \leftrightarrow \mathcal{T}(t) \rightarrow \mathrm{P}$ proceeds through $\mathcal{T}(t)$ which is a time-dependent TS. In a Markovian picture of the solvent forces, the dynamics of the reaction can be represented through a Langevin equation [72],

$$\boldsymbol{M}\,\ddot{\boldsymbol{q}} = -\boldsymbol{\Gamma}\,\dot{\boldsymbol{q}} - \nabla_{\boldsymbol{q}} V_{\mathrm{tot}}(\boldsymbol{q},t) + \boldsymbol{\xi}(t), \tag{1}$$

where $\boldsymbol{q}$ is a set of configuration variables, $\boldsymbol{M}$ is a diagonal matrix containing the masses associated with each coordinate, $\boldsymbol{\Gamma}$ is a symmetric matrix of dissipative parameters, and the stochastic term $\boldsymbol{\xi}(t)$ is uncorrelated white noise. In most cases we will study here, the stochastic term and the friction are taken such that a fluctuation-dissipation relation

$$\langle \boldsymbol{\xi}(t)\,\boldsymbol{\xi}^{\mathrm{T}}(t')\rangle = 2k_{\mathrm{B}}T\,\boldsymbol{\Gamma}\,\delta(t-t'), \tag{2}$$

is obeyed. The strength of each component of this field is varied through the independent parameters: friction and temperature.

A prototypical model for a reaction coordinate in chemical dynamics is the Eckart barrier which is often used to represent molecular reactions under stationary (gas-phase) environments. In a time-varying form

$$V(q,t) = \frac{V_0(1-\kappa)}{1+\exp[-2a(q-\mathcal{F}(t))]} + \frac{V_0(1+\sqrt{\kappa})^2}{4}\,\mathrm{sech}^2[a(q-\mathcal{F}(t))], \tag{3}$$

this energy barrier separates reactants and products along a generalized unstable reaction coordinate q which is subject to some external time-varying forcing $\mathcal{F}(t)$. The asymmetry parameter κ alters the energy difference between reactants and products. With the addition of a coupling term

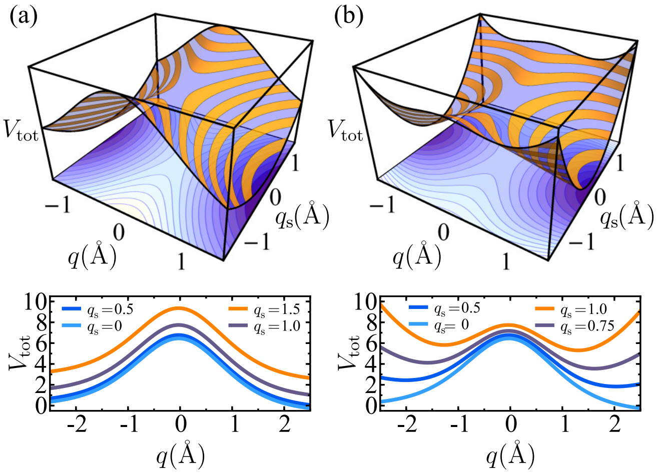

FIG. 1. Potential energy surfaces $V_{\mathrm{tot}}(q,q_{\mathrm{s}},t=0)$, given by Eq. (5), are shown for an asymmetrical Eckart system ($\kappa = 1.1$) with (a) no coupling ($V_2 = 0$) between q and q_{s} and in (b) with included coupling ($V_2 = 400\,m_{\mathrm{u}}\,\mathrm{ps}^{-2}\,\mathrm{\AA}^{-2}$). Shown below each surface is the corresponding contour plot of V. For visual clarity the axis corresponding to energy is shown in normalized units. The bottom panels show corresponding slices of V_{tot} (arbitrary units) with q_{s} held constant at the values marked in the respective legends. Parameters in all panels are $V_0 = 2000\,m_{\mathrm{u}}\,\mathrm{ps}^{-2}\,\mathrm{\AA}^2$, $V_1 = 800\,m_{\mathrm{u}}\,\mathrm{ps}^{-2}$, and $a = 0.85\,\mathrm{\AA}^{-1}$.

$$V_{\mathrm{coup}}(q,q_{\mathrm{s}},t) = \frac{V_1}{2}q_{\mathrm{s}}^2 + V_2[q-\mathcal{F}(t)]^2 q_{\mathrm{s}}^2, \tag{4}$$

where q_{s} is an auxiliary stable coordinate, the total multidimensional energy surface can be constructed as

$$V_{\mathrm{tot}}(q,q_{\mathrm{s}},t) = V(q,t) + V_{\mathrm{coup}}(q,q_{\mathrm{s}},t). \tag{5}$$

Shown in Fig. 1 are representative energy surfaces V_{tot} with q and q_{s} uncoupled ($V_2 = 0$) and coupled ($V_2 > 0$). Also shown are slices through the energy surface along q with q_{s} held constant. These slices further illustrate the geometry of the surface. We consider variations in the energy surface that result from a driving form

$$\mathcal{F}(t) = c_1\sin(\Omega_1 t) + c_2\sin(\Omega_2 t)\,, \tag{6}$$

which is bichromatic and periodic. In all cases, we take the first overtone of the fundamental frequency Ω_1 as the second frequency $\Omega_2 = 2\Omega_1$. The contributions of each frequency to the total driving form are varied through the amplitudes c_1 and c_2.

A. Parabolic approximation to the Eckart barrier

The anharmonic dynamical system consisting of a reactant particle moving on an Eckart potential energy surface in a thermal environment will serve as a basis throughout this work to illustrate the power of the LD-RG method. The harmonic limit of this system offers the possibility for validation of the use of LDs to obtain the moving TS trajectory relative to the analytical harmonic result based on the exact solution of the linear (but nonautonomous) equation of motion (EoM). To this end, we approximate the Eckart potential, given by Eq. (3), with the parabolic form

$$V(q,t) = V_0 - \frac{V_0}{4}[a^2(1+2\sqrt{\kappa}+\kappa)][q-q^*-\mathcal{F}(t)]^2, \tag{7}$$

where

$$q^* = \frac{1}{2a}\ln\left(\frac{1+\sqrt{\kappa}}{\kappa+\sqrt{\kappa}}\right) \tag{8}$$

is the shift of the energetic maximum due to asymmetry in the potential surface. For the symmetrical Eckart barrier ($\kappa = 1$), the position of the energetic barrier top (BT) has an instantaneous position $\mathcal{F}(t)$. For the case of an asymmetrical Eckart barrier the BT is shifted by the factor $q^* \neq 0$. Combining Eqs. (1) and (7) gives the EoM for a time-varying parabolic barrier in a thermal environment. This model system will serve as a paradigm for benchmarking the developed procedures, specifically for validation that through optimization of LDs, TS trajectories with associated phase space separatrices can be constructed.

B. Lagrangian descriptors

The formulation and application of LDs [67,68] has provided insight into the often complex phase space geometry in time-dependent systems. Particularly positive results have been obtained by applying LDs to the study of ocean flow currents [67], although the methodology is sufficiently general such that is not restricted to systems with such large length scales. A LD takes the general form

$$M(\boldsymbol{q}_0,t_0)_\tau = \int_{t_0-\tau}^{t_0+\tau} \mathcal{P}[\boldsymbol{q}(t)]\,dt, \tag{9}$$

where $\mathcal{P}$ is a positive quantity that accumulates as the unique trajectory $\boldsymbol{q}(t)$ evolves from point $\boldsymbol{q}_0$ at time t_0 up to time $t_0 \pm \tau$ in forward and backward time, respectively. Some examples of LDs are phase space arc length, configuration space distance, configuration space displacement, and cumulative kinetic energy. Beyond applications in fluid dynamics, Lagrangian descriptors are a simple and unique methodological tool for the study of time-dependent chemical reaction phenomena and molecular motion.

We have shown that the LD corresponding to the distance traveled in configuration space over a time τ,

$$L(\boldsymbol{q}_0,t_0) = \int_{t_0-\tau_\mathrm{b}}^{t_0+\tau_\mathrm{f}} \|\dot{\boldsymbol{q}}_c(\boldsymbol{q}_0,t_0,t)\|\,dt, \tag{10}$$

can be used to reveal hyperbolic trajectories in field-induced and thermalized chemical reactions [69–71,73,74]. The associated stable and unstable manifolds can also be obtained by separating L into forward-time (L_f) and backward-time (L_b) components and minimizing these quantities with respect to the initial conditions $\boldsymbol{q}_0$. For forward-time integration

$$L_\mathrm{f}(\boldsymbol{q}_0,t_0) = \int_{t_0}^{t_0+\tau_\mathrm{f}} \|\dot{\boldsymbol{q}}_c(\boldsymbol{q}_0,t_0,t)\|\,dt, \tag{11}$$

and in backward time,

$$L_\mathrm{b}(\boldsymbol{q}_0,t_0) = \int_{t_0-\tau_\mathrm{b}}^{t_0} \|\dot{\boldsymbol{q}}_c(\boldsymbol{q}_0,t_0,t)\|\,dt, \tag{12}$$

where the intervals of forward and backward integration are $[t_0,t_0+\tau_\mathrm{f}]$ and $[t_0-\tau_\mathrm{b},t_0]$, $\|\cdot\|$ is the norm and $\boldsymbol{q}_c$ are generalized coordinates in configuration space.

For a single reactive degree of freedom (DoF), holding the coordinate q_0 constant and minimizing with respect to $\dot{q}_0$ yields the stable manifold

$$\mathcal{W}^\mathrm{s}(q_0 = C,t_0) = \text{argmin } L_\mathrm{f}(\dot{q}_0,q_0 = C,t_0)_{R_\mathrm{f}}, \tag{13}$$

in forward time, and the unstable manifold

$$\mathcal{W}^\mathrm{u}(q_0 = C,t_0) = \text{argmin } L_\mathrm{b}(\dot{q}_0,q_0 = C,t_0)_{R_\mathrm{b}}, \tag{14}$$

in backward time, where argmin$(\cdot)$ returns the argument that minimizes the given function and $R_\mathrm{f,b}$ are suitable phase space regions about the BT that contain the respective manifold. In the absence of dissipation the integration times in Eqs. (11) and (12) can be chosen such that $\tau_\mathrm{f} = \tau_\mathrm{b}$ as the dynamical contributions in the respective time directions are on the same order. In the presence of dissipative forces the respective integration times are chosen such that strong minima are observed on the L_f and L_b surfaces. The fundamental insight leading to construction of the TS trajectory using LDs is recognizing that it is the only trajectory that remains bounded in the region of the BT as $t \to \infty$ and as $t \to -\infty$. Because it remains bounded for all time, it has extremal properties. This insight can be utilized to locate this distinguished trajectory through the optimization of LDs.

In the nonautonomous system given by Eq. (1), the manifolds associated with the TS trajectory $\boldsymbol{\mathcal{T}}$ are time dependent. After constructing $\mathcal{W}^\mathrm{s}$ and $\mathcal{W}^\mathrm{u}$, the TS trajectory can be obtained by extrapolating to the point of intersection between these two manifolds. This intersection point is an instantaneous hyperbolic point. The TS trajectory can be obtained by using this phase-space point as the initial condition and evolving this trajectory in time. Another method which we have found useful for constructing and visualizing the TS trajectory is to combine the forward- and backward-time LDs and then minimize on the resulting $L = g_\mathrm{f}L_\mathrm{f} + g_\mathrm{b}L_\mathrm{b}$, where $g_\mathrm{f,b} = e^{\pm\gamma\tau_\mathrm{w}/m}$ are weights that account for the contraction and expansion of phase space in a dissipative environment [69,74]. The phase-space coordinates of the TS trajectory can then be obtained directly by minimizing with respect to initial conditions at some t_0 on this surface,

$$\boldsymbol{\mathcal{T}}(t_0) = \text{argmin } L(\boldsymbol{q}_0,t_0)_{R_\mathrm{f}\cap R_\mathrm{b}}, \tag{15}$$

and will correspond to a minimum on the L surface.

III. PARABOLIC TRANSITION STATE TRAJECTORY

For the parabolic barrier given by Eq. (7), the TS trajectory $\boldsymbol{\mathcal{T}}(t)$ can be obtained analytically for any arbitrary motion of the energy surface $\mathcal{F}(t)$ and realization of the thermal driving. We now restrict our discussion to a one DoF model in which q is an unstable reaction coordinate. The equation of motion for this single DoF system is

$$m\ddot{q} = -\gamma\dot{q} - \frac{\partial V(q,t)}{\partial q} + \xi(t). \tag{16}$$

In this case, the TS trajectory is hyperbolic and is associated with stable and unstable manifolds $\mathcal{W}^{\mathrm{s,u}}$. The eigenvalues of the parabolic system

$$\lambda_{\mathrm{s},u} = -\frac{1}{2m}\left[\gamma \pm \sqrt{\gamma^2 + 2ma^2V_0(1+2\sqrt{\kappa}+\kappa)}\right] \tag{17}$$

correspond to the stable and unstable manifolds, respectively. Each eigenvalue carries units of inverse time. In a dissipative system, they satisfy $\lambda_{\mathrm{s}} + \lambda_{\mathrm{u}} = -\gamma/m$. This factor describes the stretching or contraction rate of phase-space volume in forward or backward time, respectively.

The dynamical system can now be defined on a moving hyperbolic point using a method proposed by Bartsch *et al.* [41,42,65,66] through the use of the S functionals,

$$S_\tau[\mu,g;t] = \begin{cases} -\int_t^{\infty} g(\tau)\,\exp[\mu(t-\tau)]\,d\tau : & \mathrm{Re}\,\mu > 0, \\ +\int_{-\infty}^{t} g(\tau)\,\exp[\mu(t-\tau)]\,d\tau : & \mathrm{Re}\,\mu < 0, \end{cases} \tag{18}$$

whose argument includes the decay rate μ and driving force g. The S functionals suppress the exponential factors in the solution of the EoM and return the bounded portion. The TS trajectory of the system defined by combining Eqs. (1) and (7) is therefore given by

$$\mathcal{T}(t) = \frac{1}{\lambda_{\mathrm{u}} - \lambda_{\mathrm{s}}}\left[\frac{a^2V_0(1+2\sqrt{\kappa}+\kappa)}{2m}(S[\lambda_{\mathrm{s}},\mathcal{F};t] - S[\lambda_{\mathrm{u}},\mathcal{F};t]) + \frac{\sqrt{2\sigma}}{m}(S[\lambda_{\mathrm{s}},\xi;t] - S[\lambda_{\mathrm{u}},\xi;t])\right] + q^*, \tag{19}$$

$$\dot{\mathcal{T}}(t) = \frac{1}{\lambda_{\mathrm{u}} - \lambda_{\mathrm{s}}}\left[\frac{a^2V_0(1+2\sqrt{\kappa}+\kappa)}{2m}(\lambda_{\mathrm{s}}S[\lambda_{\mathrm{s}},\mathcal{F};t] - \lambda_{\mathrm{u}}S[\lambda_{\mathrm{u}},\mathcal{F};t]) + \frac{\sqrt{2\sigma}}{m}(\lambda_{\mathrm{s}}S[\lambda_{\mathrm{s}},\xi;t] - \lambda_{\mathrm{u}}S[\lambda_{\mathrm{u}},\xi;t])\right], \tag{20}$$

which depends on the particular realization of the deterministic driving $\mathcal{F}(t)$ and the specific noise sequence $\xi(t)$. Equations (19) and (20) define the TS trajectory in the unstable (reactive) degree of freedom.

Correspondence between optimization of *L* and the TS trajectory

The TS trajectory associated with a moving parabolic system remains bounded within the domain of time-dependent barrier top positions in both the infinite future and the infinite past. If the barrier movement is periodic, then the TS trajectory will likewise be periodic. As shown in Fig. 2(a), for athermal periodic driving the resulting TS trajectory is a periodic orbit $\mathcal{O}$ [59]. In this case, using the methods described in Sec. II B, optimization of $L_{\mathrm{f,b}}$ yields the same trajectory as $\mathcal{O}$. With the inclusion of thermal driving and dissipation, the corresponding TS trajectories determined by Eqs. (19) and (20), and those obtained through optimization of the Lagrangian descriptors are in excellent agreement, as can be seen in Fig. 2. This numerical agreement is suggestive of the accuracy of the latter procedure in obtaining the TS trajectory [57–59,69].

IV. REACTION MANIFOLDS

A. Parabolic barrier

The stable and unstable manifolds of a parabolic energy barrier can be readily characterized in the moving frame associated with the TS trajectory. The eigenvectors of the EoM in this moving frame correspond to the stable and unstable manifolds, while the moving frame itself depends on the realization of the deterministic driving $\mathcal{F}$ and the specific noise sequence ξ. For the case of an athermal stationary barrier with a linear EoM, the fixed point $\boldsymbol{\mathcal{T}} = (q^*,0)$ corresponds to the traditional picture of the transition state, and the stable and unstable manifolds of $\boldsymbol{\mathcal{T}}$ are also linear [15]. In the case of time-varying parabolic surface in a thermal environment the manifolds associated with $\boldsymbol{\mathcal{T}}(t)$ are time dependent and described by

$$\mathcal{W}^{\mathrm{s}}(\boldsymbol{\mathcal{T}}(t)) : \{(\dot{q} - \dot{\mathcal{T}}(t)) - \lambda_{\mathrm{s}}(q - \mathcal{T}(t)) = 0\}, \tag{21}$$

$$\mathcal{W}^{\mathrm{u}}(\boldsymbol{\mathcal{T}}(t)) : \{(\dot{q} - \dot{\mathcal{T}}(t)) - \lambda_{\mathrm{u}}(q - \mathcal{T}(t)) = 0\}. \tag{22}$$

Several cases are explored below to provide additional illustration of the structure of the TS trajectory and the accuracy of the Lagrangian descriptor scheme in describing the associated manifolds.

We first examine the applicability of minimizing $L_{\mathrm{f,b}}$ to construct the corresponding manifolds on autonomous Hamiltonian and autonomous dissipative systems. While this is a trivial system in which to construct the reaction geometry, it will serve as an excellent benchmark for the LD method described in Sec. II B. In a parabolic system, the stable and unstable manifolds are defined by the lines spanned by the corresponding eigenvectors of the linearized EoM about the fixed point $\boldsymbol{\mathcal{T}}$. As shown in Fig. 3, $\boldsymbol{\mathcal{T}}$ corresponds to a strong minima on the L surface. This is the expected results because a trajectory with these initial conditions will have $L_{\mathrm{f,b}} = 0$ by definition of a fixed point.

The stable and unstable manifolds associated with $\boldsymbol{\mathcal{T}}$ can be constructed through minimization of $L_{\mathrm{f,b}}$. This can be seen in Fig. 4 where the optimization procedure leads to excellent agreement with the exact analytical values of the corresponding manifolds. Note that the effect of dissipation causes a rotation in the manifolds, and an increase in the so-called critical

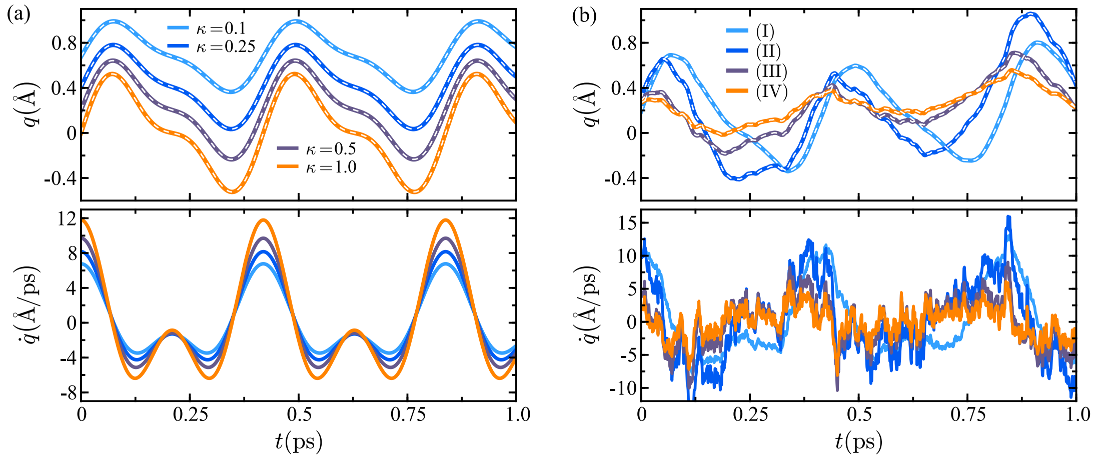

FIG. 2. Components of the TS trajectory, $\mathcal{T}$ (top) and $\dot{\mathcal{T}}$ (bottom) for (a) athermal and (b) thermal systems and varying values of κ, γ, and T. The exact TS trajectories given by Eqs. (19) and (20) are shown as solid curves. The configuration space component of $\mathcal{T}$ found through the LD-RG procedure discussed in the main text is shown as a dashed curve (white) in each top panel. For each trajectory in (b), $\kappa = 0.5$ and the thermal parameters are as follows: (I) $\gamma = 25\,m_{\mathrm{u}}/\mathrm{ps}$, $T = 298\,\mathrm{K}$; (II) $\gamma = 250\,m_{\mathrm{u}}/\mathrm{ps}$, $T = 298\,\mathrm{K}$; (III) $\gamma = 725\,m_{\mathrm{u}}/\mathrm{ps}$, $T = 100\,\mathrm{K}$; and (IV) $\gamma = 1250\,m_{\mathrm{u}}/\mathrm{ps}$, $T = 50\,\mathrm{K}$. Parameters in all panels are $m = 10\,m_{\mathrm{u}}$, $c_1 = c_2 = 0.75\,\text{Å}$, $\Omega_1 = 15\,\mathrm{ps}^{-1}$, and $a = 0.85\,\text{Å}^{-1}$.

velocity [65,66,75] $V^{\ddagger}$ which separates reactive and nonreactive regions of phase space for trajectories with initial position q_0 held constant. Trajectories that have an initial velocity $\dot{q}_0 > V^{\ddagger}$ are reactive and trajectories with $\dot{q}_0 < V^{\ddagger}$ are nonreactive. The effect of dissipation raises this value as a dissipative environment removes energy from the system and a trajectory must be launched with greater energy in order to surmount the barrier. The corresponding LDs capture this behavior.

The agreement between the minimization of $L_{\mathrm{f,b}}$ and the exact values of $\mathcal{W}^{\mathrm{s,u}}$ is further illustrated in Fig. 5 where, by construction of $L_{\mathrm{f,b}}(q,\dot{q})$ with q held constant, a strong minima is observed on the Lagrangian surface at the location

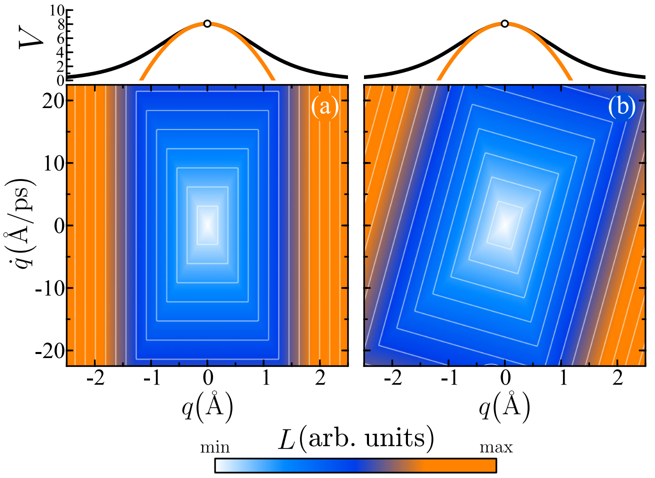

FIG. 3. Phase-space contour plots of the sum L of the forward and backward LDs are shown in (a) for a symmetrical barrier ($\kappa = 1$, $\gamma = 0$) and in (b) for a symmetrical barrier ($\kappa = 1, \gamma = 250\,m_{\mathrm{u}}/\mathrm{ps}$) in a dissipative environment. The values of the range from minimum to maximum are noted in the color (gray) bar. Both systems are noiseless. The fixed point of both systems $\mathcal{T}$ is shown as a circular marker on the time-varying potential surface (above), which is shown in units of $k_{\mathrm{B}}T$ at 298 K, with the Eckart barrier shown in black and the parabolic approximation shown in orange (gray). Parameters in all panels are $\tau = 0.5\,\mathrm{ps}$, $\tau_{\mathrm{w}} = 0.23\,\mathrm{ps}$, $m = 10\,m_{\mathrm{u}}$, and $a = 0.85\,\text{Å}^{-1}$.

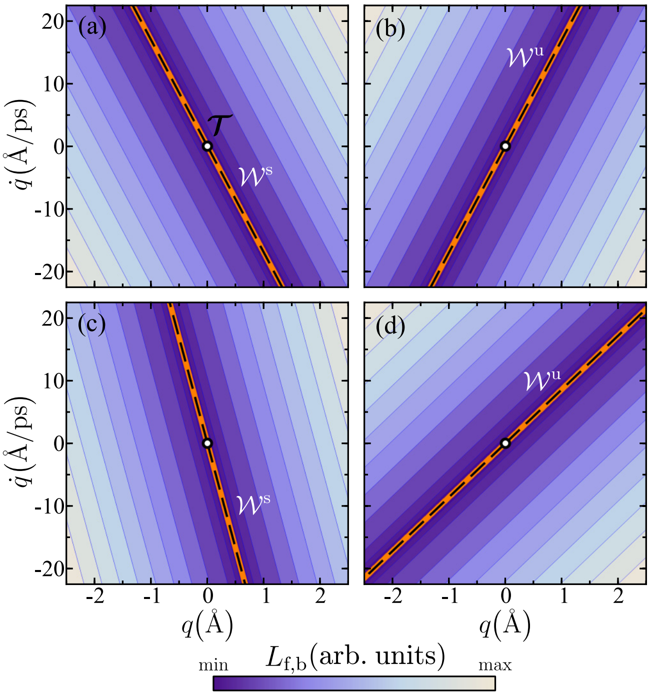

FIG. 4. Phase-space contour plots of L_{f} and L_{b} are shown respectively in panels (a) and (b) for a symmetrical barrier ($\kappa = 1$, $\gamma = 0$) and in panels (c) and (d) for a symmetrical barrier ($\kappa = 1$, $\gamma = 250\,m_{\mathrm{u}}/\mathrm{ps}$) in a dissipative environment. The values of the range from minimum to maximum are noted in the color (gray) bar. Both systems are noiseless. The fixed point of both systems $\mathcal{T}$ is shown as a circular marker. The corresponding stable $\mathcal{W}^{\mathrm{s}}$ and unstable $\mathcal{W}^{\mathrm{u}}$ manifolds calculated through minimization of $L_{\mathrm{f,b}}$ are shown as solid orange (light gray) lines. They are overlaid by the exact manifolds shown as dashed lines (black). The number of contours is increased in the vicinity of the manifold to illustrate convergence to the minimum. Remaining parameters are the same as in Fig. 3.

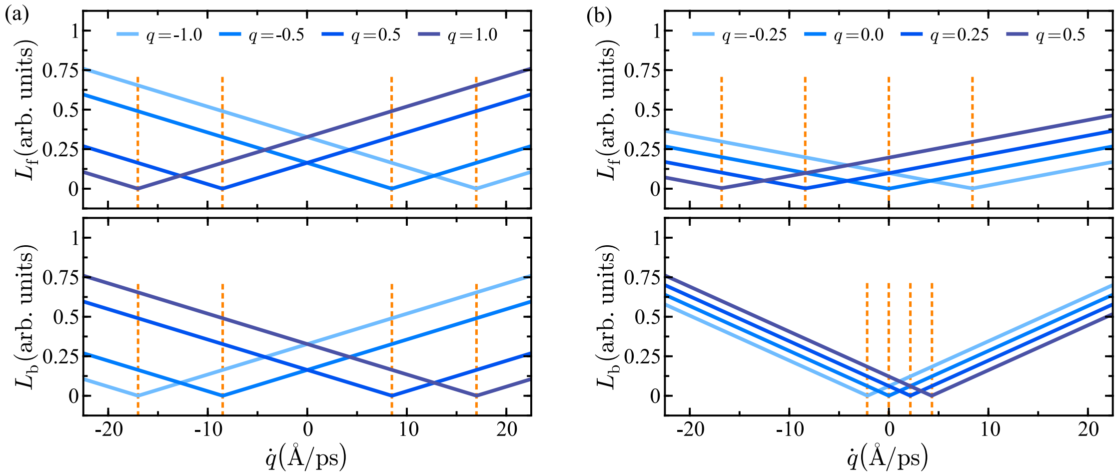

FIG. 5. Calculation of L_f (top) and L_b (bottom) for varying initial conditions $\boldsymbol{q}_0 = (q,\dot{q})$, with q held constant at the values given in the legend are shown in (a) for a stationary symmetrical barrier and in (b) for a stationary symmetrical barrier in a dissipative environment ($\gamma = 250\,m_\mathrm{u}$/ps). Both systems are noiseless. The exact value of the respective manifold is marked by a orange (gray) vertical dashed line. Additional parameters in all panels are as in Fig. 3.

of the corresponding manifold. This minima is in excellent agreement with the exact position of the respective manifold, further supporting the argument that through minimization of $L_\mathrm{f,b}$ the respective manifolds can be recovered.

A constructive proof of the claim that the manifolds of a parabolic system can be obtained using LDs is provided below through the explicit evaluation of Eqs. (13) and (14). For simplicity, we consider a stationary and conservative system by setting $\gamma = 0$ and removing the forcing term $\mathcal{F}(t)$. In the stationary setting, the EoM is

$$\ddot{q} = \omega^2(q - q^*), \tag{23}$$

where

$$\omega = \sqrt{\frac{V_0}{2m}[a^2(1 + 2\sqrt{\kappa} + \kappa)]}. \tag{24}$$

We first construct the stable manifold associated with the fixed point $\mathcal{T} = (q^*,0)$. The unstable manifold can be constructed using similar arguments to avoid being overly pedantic. Solving Eq. (23) yields

$$q(\boldsymbol{q}_0,t) = (q_0 - q^*)\cosh(\omega t) + \frac{\dot{q}_0}{\omega}\sinh(\omega t) + q^*,$$
$$\dot{q}(\boldsymbol{q}_0,t) = \dot{q}_0\cosh(\omega t) + (q_0 - q^*)\omega\sinh(\omega t). \tag{25}$$

The phase space of this system can be partitioned into quadrants using the lines $\dot{q} = 0$ and $q = q^*$. In quadrants I and III: $\mathrm{sgn}\,(q_0 - q^*) = \mathrm{sgn}\,(\dot{q}_0)$ and in quadrants II and IV: $\mathrm{sgn}\,(q_0 - q^*) \neq \mathrm{sgn}\,(\dot{q}_0)$. The stable manifold exists in quadrants II and IV, so we now confine our discussion to these quadrants.

There are two types of trajectories that are not part of the manifold network: reactive and nonreactive. Reactive trajectories are defined by the set of initial conditions that begin on the reactant side of the dividing surface, and move to the product side in forward-time. For backward-time integration, reactive trajectories move from the product side to the reactant side. Nonreactive trajectories approach the barrier top, change sign in velocity and stay on the reactant side (product side in backward time). The time where this velocity sign change occurs, t_c, can be obtained by solving

$$\dot{q}(\boldsymbol{q}_0,t) = 0, \tag{26}$$

for t, which gives

$$t_c = \frac{1}{2\omega}\ln\left[\frac{(q_0 - q^*)\omega - \dot{q}_0}{(q_0 - q^*)\omega + \dot{q}_0}\right]. \tag{27}$$

Equation (27) has a positive asymptote at $\dot{q}_0 = -\omega(q_0 - q^*)$ which defines the corresponding initial velocity $\dot{q}_0$ for position $q = (q_0 - q^*)$ such that the trajectory is on the stable manifold.

We use minimized LDs to obtain the stable manifold. By confining our discussion to quadrants II and IV, t_c has the property $\mathrm{Re}\,t_c \geqslant 0$, which means that, e.g., in quadrant II, a trajectory either crosses the DS in forward time (reactive) or does not cross at all (nonreactive). The absolute value function $\|\dot{q}(\boldsymbol{q}_0,t_0,t)\|$ in the integral L_f can be separated into intervals before and after t_c, and the solution in quadrants II and IV can be written as:

$$L_\mathrm{f}(\boldsymbol{q}_0,\tau) = \begin{cases} \lim_{t'\to t_c^-}\int_0^{t'}\|\dot{q}(\boldsymbol{q}_0,t)\|\,dt + \lim_{t'\to t_c^+}\int_{t'}^{\tau}\|\dot{q}(\boldsymbol{q}_0,t)\|\,dt & \\ \quad = -\frac{(q_0-q^*)\sqrt{\dot{q}_0^2}}{\dot{q}_0} - \frac{2\sqrt{\omega^2(q_0-q^*)^2-\dot{q}_0^2}}{\omega} + \frac{(q(\boldsymbol{q}_0,\tau)-q^*)\sqrt{\dot{q}^2(\boldsymbol{q}_0,\tau)}}{\dot{q}(\boldsymbol{q}_0,\tau)} : & \mathrm{Im}\,t_c = 0 \text{ and } \tau > t_c, \\ \int_0^{\tau}\|\dot{q}(\boldsymbol{q}_0,t)\|\,dt = -\frac{(q_0-q^*)\sqrt{\dot{q}_0^2}}{\dot{q}_0} + \frac{(q(\boldsymbol{q}_0,\tau)-q^*)\sqrt{\dot{q}^2(\boldsymbol{q}_0,\tau)}}{\dot{q}(\boldsymbol{q}_0,\tau)} : & \mathrm{Im}\,t_c \neq 0 \text{ or } \mathrm{Im}\,t_c = 0 \text{ and } \tau < t_c. \end{cases} \tag{28}$$

In a stationary environment the choice of t_0 in Eq. (13) is arbitrary, and here we have set $t_0 = 0$ for simplicity. Note that for a specific q_0, the change from nonreactive to reactive trajectories, and thus from regions where $\mathrm{Im}\,t_c = 0$ to $\mathrm{Im}\,t_c \neq 0$, occurs at the stable manifold.

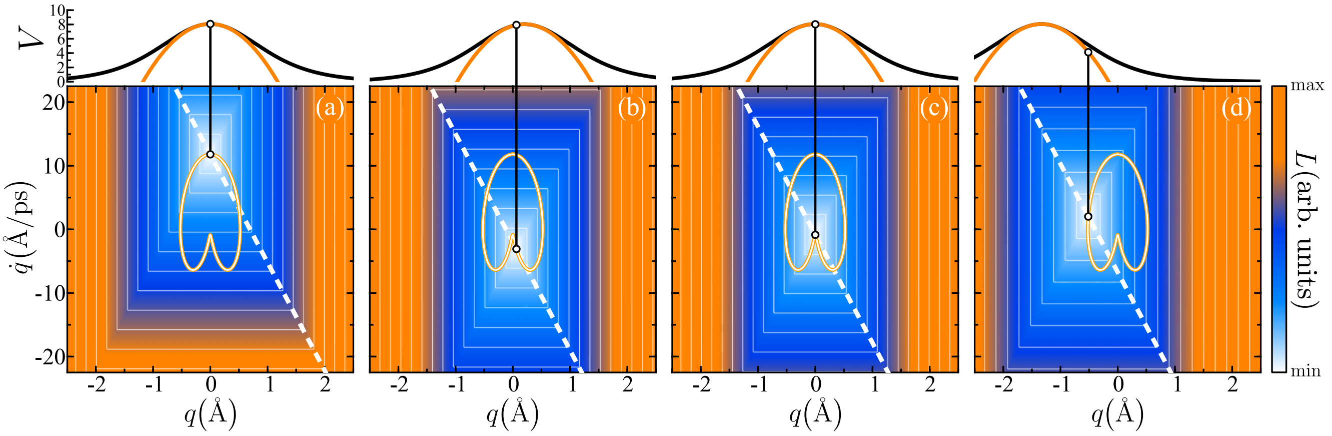

FIG. 6. Phase-space contour plots of $L(\boldsymbol{q}_0,t_0)$ for $t_0 \in \{0,0.125,0.209,0.356\}$ are shown in (a)–(d) for a time-varying athermal symmetrical barrier ($\kappa = 1,\gamma = 0$). In all panels, the TS trajectory $\mathcal{T}(t)$ is shown as a light-orange (light gray) striped curve over an entire period of oscillation and the stable manifold at time t_0 is shown as a dashed curve (white). The time-varying potential surface is shown above in units of $k_\mathrm{B}T$ at 298 K, with the Eckart barrier shown in black and the parabolic approximation shown in orange (gray). In all panels, $\tau = 0.5$ ps and additional parameters are as in Fig. 2.

We wish to minimize L_f with respect to $\dot{q}_0$ while holding q_0 constant. This is accomplished by solving

$$\frac{\partial L_\mathrm{f}(\boldsymbol{q}_0,\tau)}{\partial \dot{q}_0} = 0, \tag{29}$$

for $\dot{q}_0$ and sorting the appropriate root. The initial velocity that solves Eq. (29) minimizes L_f and we denote this velocity $\dot{q}_0^{(\mathrm{s})}$ as it will be used to obtain the stable manifold. After some algebraic manipulation we obtain

$$\dot{q}_0^{(\mathrm{s})}(\tau) = -\omega(q_0 - q^*)\sqrt{\frac{\sinh^2(\omega\tau)}{4+\sinh^2(\omega\tau)}}, \tag{30}$$

which is a function of τ (the integration time). In the limit $\tau \to \infty$ the exact value of the stable manifold is recovered,

$$\lim_{\tau\to\infty} \dot{q}_0^{(\mathrm{s})}(\tau) = -\omega(q_0 - q^*), \tag{31}$$

and thus we have proven that Eq. (13) tends to the stable manifold as $\tau \to \infty$. This value is in agreement with the vertical asymptote of t_c and the calculation given by Eq. (21). The unstable manifold can be constructed using similar arguments in backward time.

We have thus far illustrated the use of LDs in autonomous systems; however, the methodology is also applicable in nonautonomous systems such as thermalized chemical reactions that occur in a Langevin-type bath [69] and reactions that are driven by external fields [71]. Using LDs to construct and visualize the underlying phase space geometry in time-dependent systems is perhaps their most useful application.

In thermalized systems on time-varying energy surfaces, the structure of the TS trajectory, and its associated manifolds, depends on the specific form of the external driving, and also on the geometry of the noise. For a periodically varying parabolic surface in an athermal environment ($T \to 0$), the corresponding TS trajectory is an unstable periodic orbit that remains bounded in the vicinity of the BT region for all time (see Sec. III A) [59]. Constructing this object with an LD minimization scheme yields $\mathcal{T}(t)$, as shown in Fig. 6. Note that the configuration space component of the TS trajectory $\mathcal{T}$ does not correspond to the instantaneous BT, i.e., $\mathcal{T}$ does not correspond to the traditional view of the transition state. The relation between $\mathcal{T}$ and the position of BT at varying times is illustrated in each panel in Fig. 6. With the inclusion of noise and dissipation, the TS trajectory of Eq. (16) is no longer smoothly varying and is a function of both the external driving form $\mathcal{F}(t)$ controlling the time evolution of the energy surface, and also the noise. However, for a parabolic barrier, the EoM remains linear and thus the manifolds associated with $\mathcal{T}(t)$ are also linear. As shown in Fig. 7, in this case, the TS trajectory can once again be recovered through the use of the LD minimization scheme, with the instantaneous phase space position of $\mathcal{T}$ at time t_0 given by locating the conical point on $L(\boldsymbol{q}_0,t_0)$.

B. Eckart barrier

Lagrangian descriptors can also be applied to construct the reaction manifolds of anharmonic barriers. As illustrated in Fig. 8 for a stationary Eckart barrier, the general trends are the same as in the parabolic case. Namely, the ridge lines of L still mark separatrices dividing reactants and products, and the intersection $\mathcal{T}$ of the manifolds is the instantaneous position of the TS. Note in Fig. 8(b) the shift of the BT position by a factor q^* due to asymmetry in the potential surface. Meanwhile, the L surface no longer exhibits the linear structure we saw in the parabolic cases of Figs. 3 and 4. This gives rise to curved separatrices for the anharmonic Eckart potential. The effect of dissipation on the manifold geometry is shown in Figs. 8(c) and 8(d). In this case, due to loss of energy into the thermal bath, a trajectory must have a larger initial velocity with respect to the corresponding conservative system to change from a reactant to product state. This results in a rotation of the stable manifold and the Lagrangian surface constructed using LDs captures this behavior.

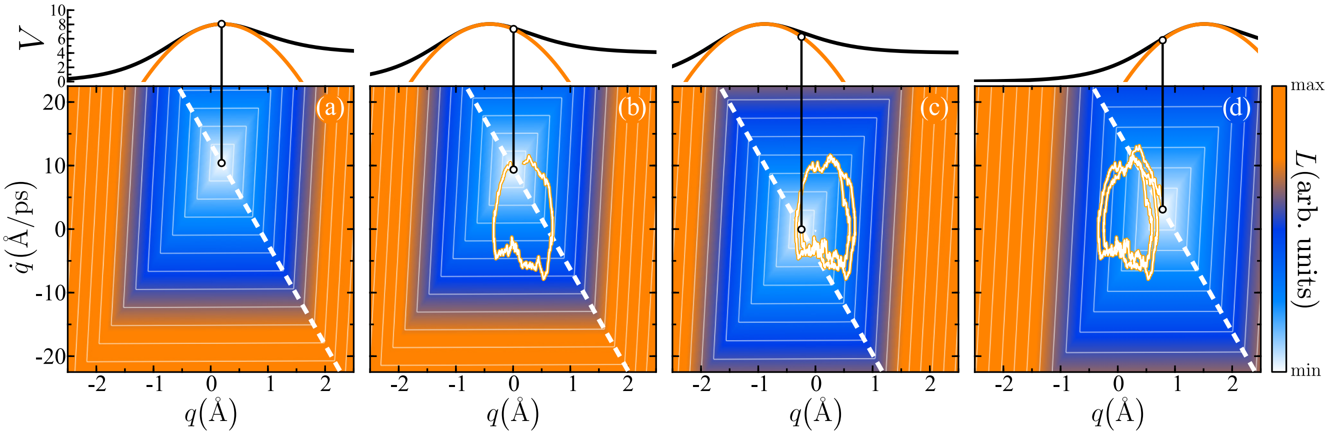

FIG. 7. Phase-space contour plots of $L(\boldsymbol{q}_0,t_0)$ for $t_0 \in \{0,0.4,0.75,0.9\}$ are shown in (a)–(d) for a time-varying thermalized asymmetrical barrier ($\kappa = 0.5, \gamma = 25\, m_{\mathrm{u}}/\mathrm{ps}$). In all panels, the TS trajectory $\boldsymbol{\mathcal{T}}(t)$ is shown as a light-orange (light gray) striped curve over the interval $[0,t_0]$ and the stable manifold at time t_0 is shown as a dashed curve (white). The time-varying potential surface is shown above in units of $k_{\mathrm{B}}T$ at 298 K, which is the temperature of the thermal bath, with the Eckart barrier shown in black and the parabolic approximation shown in orange (gray). Parameters in all panels are $\tau = 0.5$ ps and $\tau_{\mathrm{w}} = 0.22$ ps. Additional parameters in all panels are as in Fig. 2.

Differences in the structure of $L_{\mathrm{f,b}}$ on harmonic and anharmonic surfaces can also be observed by comparing slices through the corresponding surfaces in Fig. 5 for a harmonic barrier and in Fig. 9 for the Eckart barrier. Variation of $\dot{q}_0$ with q_0 held constant leads to nonlinear behavior in $L_{\mathrm{f,b}}$ for an Eckart barrier, and linear behavior for a harmonic barrier. Note that the location of the manifold for a specific q_0 value corresponds to the minimum on the respective curve shown in Fig. 9 and this observation is in agreement with Eqs. (13) and (14).

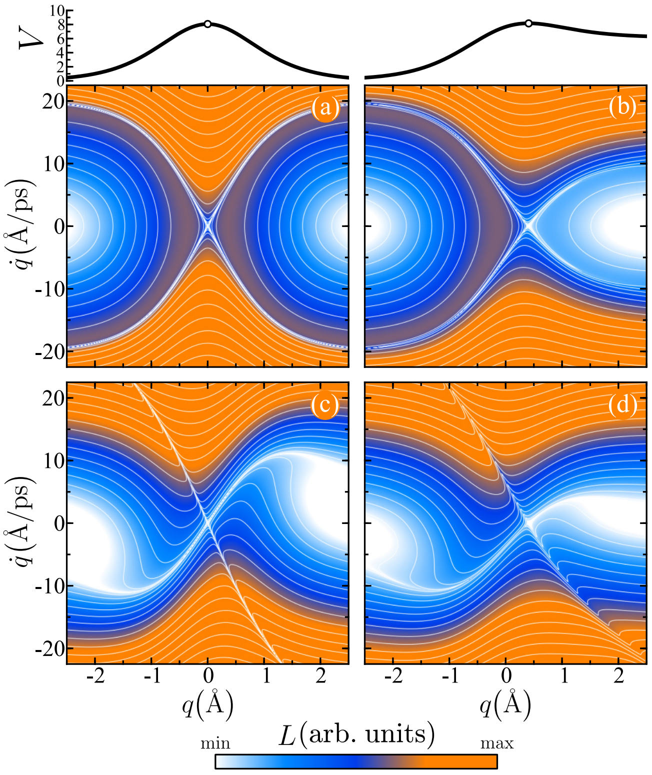

FIG. 8. Phase-space contour plots of the sum L of the forward and backward LDs of autonomous systems are shown in (a) for a symmetrical Eckart barrier ($\kappa = 1$) and in (b) for a asymmetrical Eckart barrier ($\kappa = 0.25$). Panels (c) and (d) display contour plots of the respective symmetrical and asymmetrical systems are shown for dissipative environments ($\gamma = 75\, m_{\mathrm{u}}/\mathrm{ps}$). The time-varying potential surface is shown in units of $k_{\mathrm{B}}T$ at 298 K in the top unlabeled panels. Open circles highlight the fixed point $\boldsymbol{\mathcal{T}}$ of each system. Parameters in all panels are $\tau = 0.5$ ps, $\tau_{\mathrm{w}} = 0.15$ ps, and $m = 10\, m_{\mathrm{u}}$.

The manifold network geometry for a nonautonomous anharmonic system is shown in Fig. 10 using a time-varying Eckart barrier in a thermal environment as a representative model. As in the autonomous case, strong ridges are observed on the $L_{\mathrm{f,b}}$ surfaces which mark the location of the respective stable-unstable manifold. The correspondence (or lack thereof) between the stable and unstable manifolds of the moving hyperbolic point $\boldsymbol{\mathcal{T}}$ and the time-varying geometry of the potential energy surface can be seen by comparing the Lagrangian surfaces in Fig. 10 with the corresponding potentials shown above each panel. In anharmonic systems, the time dependence of the manifolds is not only manifested in translation associated with the moving hyperbolic point, but the topology of the manifolds themselves is also time dependent in the static coordinate system, as observed in Fig. 10.

C. Multidimensional dynamics

We now consider the case of a multidimensional reactive system by coupling the reactive degree of freedom to a harmonic bath mode q_{s} as represented by the two-dimensional potential in Eq. (5). Inclusion of the stable bath coordinate leads to a manifold geometry with higher dimensionality that is significantly more complex. However, the minimum valleys of the forward and backward LD surfaces $L_{\mathrm{f,b}}$ will still correspond to the (un)stable manifolds $\mathcal{W}^{\mathrm{s,u}}$, respectively. These multidimensional structures are illustrated here for an Eckart barrier. The lack of bounded reactant or product regions simplifies the analysis slightly, but this is not a restriction to the theory as we have also examined an athermal field-driven potential energy surface with bounded metastable states [71].

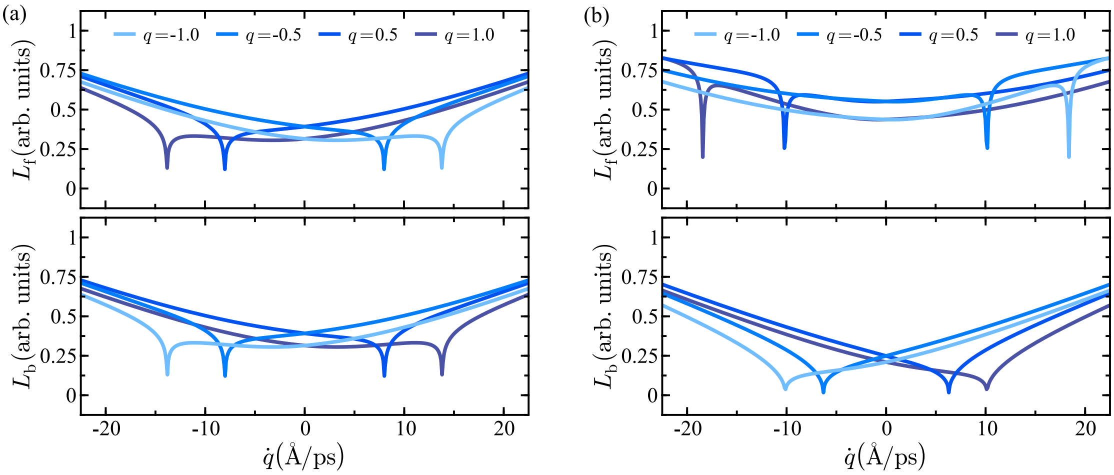

FIG. 9. Calculation of L_f (top) and L_b (bottom) for varying initial conditions $\boldsymbol{q}_0 = (q,\dot{q})$, with q held constant at the values given in the legend are shown in (a) for a stationary symmetrical Eckart barrier and in (b) for a stationary symmetrical Eckart barrier ($\gamma = 75\, m_u$/ps) in a dissipative environment. Additional parameters in all panels are as in Fig. 3.

The geometric structure of $L_{f,b}$ corresponds to the respective manifold network. This is confirmed by comparing the Lagrangian surface with the final-state basins constructed from mapping each position in phase space to a final state at time τ which is either reactive (surmounts the energy barrier) or nonreactive (does not surmount the energy barrier). The forward-time surfaces L_f in Fig. 11 are determined over the unstable coordinate [71] for different parameters and the complementary final-state basin mapping. The similarity between Figs. 11(a) and 11(e) confirms that the minimum valley on L_f separates reactive and nonreactive regions for the case of uncoupled dynamics. That is, this structure corresponds to the stable manifold in the independent unstable coordinate. The Lagrangian surfaces for the coupled dynamics between the unstable and stable coordinates are shown in Figs. 11(b)–11(d) and can be compared with the corresponding final-state basins shown in Figs. 11(f)–11(h). In all cases presented here, the L_f surface contains distinctive local minima, and these valleys coincide with the basin boundaries. This correspondence persists in phase-space slices that contain manifold structures

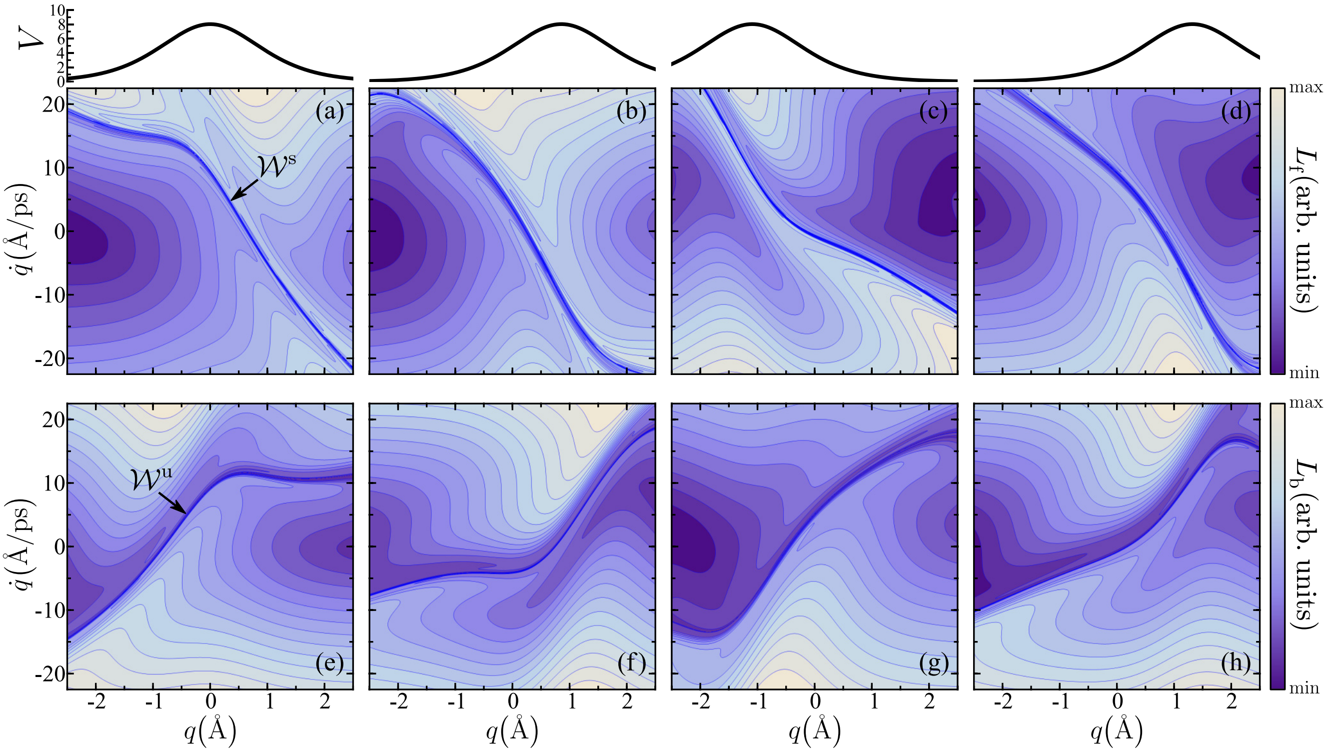

FIG. 10. Phase-space contour plots of $L_f(\boldsymbol{q}_0,t_0)$ (top) and $L_b(\boldsymbol{q}_0,t_0)$ (bottom) at $t_0 \in \{0,0.1,0.75,0.9\}$ for a time-varying thermalized symmetrical barrier ($\kappa = 1.0, \gamma = 25\, m_u$/ps) are shown in panels (a)–(d) and panels (e)–(h), respectively. The temperature of the thermal bath is 298 K and the integration time is $\tau = 1.0$ ps. Additional parameters in all panels are as in Fig. 2.

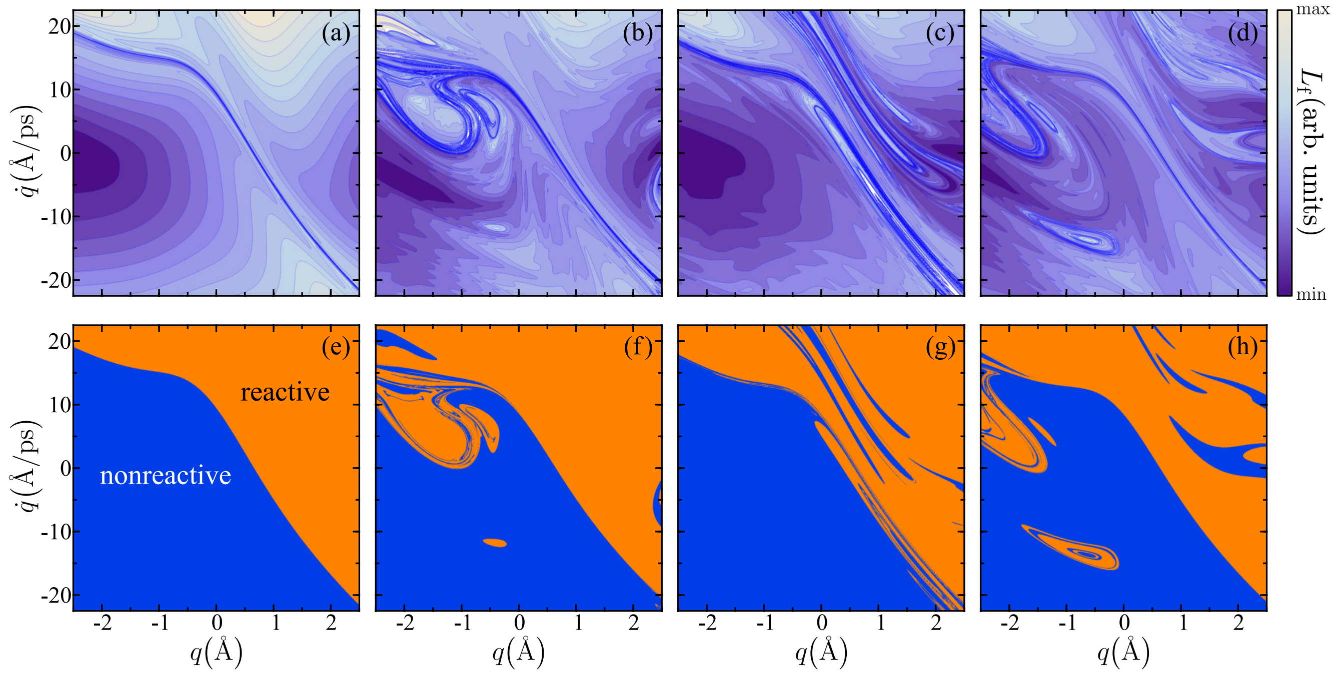

FIG. 11. Phase-space plots of $L_\mathrm{f}(\boldsymbol{q}_0,t_0)$ (top) and the corresponding final-state basins (bottom) for a two-dimensional barrier—Eckart potential in q and harmonic in q_s at $t_0 = 0$ with parameters: $\kappa = 1.0, \gamma = 25\,m_\mathrm{u}/\mathrm{ps}, T = 298\,\mathrm{K}$. Shown are phase-space portraits of the unstable mode $(q,\dot{q})$ for (a) uncoupled ($V_2 = 0$) and (b)–(d) coupled ($V_2 = 400\,m_\mathrm{u}\,\mathrm{ps}^{-2}\,\text{Å}^{-2}$) motion between unstable and stable modes with initial values of the stable mode: (b) $q_\mathrm{s} = 0.5\,\text{Å}, \dot{q}_\mathrm{s} = 0$; (c) $q_\mathrm{s} = 0, \dot{q}_\mathrm{s} = -10\,\text{Å/ps}$; (d) $q_\mathrm{s} = 0, \dot{q}_\mathrm{s} = 10\,\text{Å/ps}$. The corresponding basins shown below each L_f surface illustrate areas of phase space that are nonreactive in blue (dark gray), and reactive in orange (light gray). In all panels, the integration time is $\tau = 2.0\,\mathrm{ps}$ and additional parameters are as in Figs. 1 and 2.

with complex geometry. The observation that the final-state basin boundaries are in strong agreement with valleys on the Lagrangian surface opens the possibility that LDs can be used to construct the manifold network of a multidimensional TS, even when the barrier geometry is time varying and the reaction occurs in a thermal environment [76].

In general, the manifolds $\mathcal{W}^{\mathrm{s,u}}$ are high-dimensional objects. Depending on the location of the saddle in phase space, the orientation of its (un)stable directions, as well as the particular form of the coupling and the external driving, the (un)stable manifolds $\mathcal{W}^{\mathrm{s,u}}$ may, of course, also be observable along different coordinate axes and in different slices through the high-dimensionality phase space. For example, in the present case of an unstable Eckart barrier coupled with a stable harmonic mode, Lagrangian surfaces in the stable coordinate exhibit the typical structure seen in the vicinity of stable points.

V. CONCLUSIONS AND OUTLOOK

In this paper, we have used Lagrangian descriptors to construct separatrices, hyperbolic trajectories, and surfaces of no return in a physical system—driven by the Eckart potential—that is a standard model for thermal barrier crossing reactions in chemistry and chemical physics. A central result in this work is the proof that minimization of the Lagrangian descriptors leads exactly to manifolds of the TS trajectory in the case of harmonic barriers. This LD-RG method is applicable across many activated dynamical systems in and it can be used to provide key insight into reaction or transition processes, including, as we have shown here, in thermalized systems with many degrees of freedom.

The LD-RG theory has been illustrated for a Markovian solvent, although based on the lack of simplifying assumptions, we conjecture that it is readily extendable to reactions in structured solvents. By altering the time-dependent transition states associated with hyperbolic trajectories [77] to give specific reaction outcomes, the results presented here provide for the possibility of future developments toward optimal control of selectivity in field-driven and solvent-mediated reactions [48,78].

We are currently pursuing these methods to address reactions in solvent environments with cavitational heterogeneity [79], and specifically to coarse-grained mesoscale dynamics in which the underlying solvent has intrinsic softness [80–85]. Such systems are not presently amenable to analytic treatments because the mean-field representations of microscopic systems are not exactly renormalizable at the mesoscale. Our preliminary results show that variations in solvent softness—i.e., deformable solvent environments—manifest in alterations of the reaction geometry and subsequently the rates of the underlying reaction mechanics.

Reaction rates can be derived using the Lagrangian descriptor method in multiple ways. A brute force calculation can be performed by numerically integrating large numbers of trajectories and calculating the reactive flux through the moving dividing surface as was done in Ref. [44] using the perturbation theory-based TS trajectory. The rate constants obtained from this method approach the exact classical rates as the number of trajectories is increased because the dividing surface constructed using Lagrangian descriptors is recrossing-free [58]. In the long-time limit with respect to the decay of the reactive flux, the rates can be derived from the stability exponents (i.e., Lyapunov or Floquet exponents) of the TS trajectory [57,60]. This method minimizes the computational resources needed to obtain the rates by reducing a calculation that uses a large number of trajectories to one that uses a single trajectory, but it does not capture the decay rate of the reactive flux in the short-time limit. A more robust method for the calculation of the flux integrals in the usual TST expression of the rate constant would use the moving dividing surface obtained from the LD-RG theory.

ACKNOWLEDGMENTS

This work has been supported by the Air Force Office of Scientific Research through Grant No. FA9550-12-1-0483. A.J. acknowledges the Alexander von Humboldt Foundation, Germany, for support through a Feodor Lynen Fellowship.

[1] C. Jarzynski, Nat. Phys. **11**, 105 (2015).
[2] J. R. Green, A. B. Costa, B. A. Grzybowski, and I. Szleifer, Proc. Natl. Acad. Sci. USA **110**, 16339 (2013).
[3] S. Saha and J. F. Stoddart, Chem. Soc. Rev. **36**, 77 (2007).
[4] J. Michl and E. C. H. Sykes, ACS Nano **3**, 1042 (2009).
[5] C. Zazza, G. Mancini, G. Brancato, and V. Barone, J. Phys. Chem. Lett. **4**, 3885 (2013).
[6] J. Morfill, J. Neumann, K. Blank, U. Steinbach, E. M. Puchner, K.-E. Gottschalk, and H. E. Gaub, J. Mol. Biol. **381**, 1253 (2008).
[7] H. Gelman, M. Platkov, and M. Gruebele, Chem. Eur. J. **18**, 6420 (2012).
[8] A. J. Wirth, M. Platkov, and M. Gruebele, J. Am. Chem. Soc. **135**, 19215 (2013).
[9] M. Platkov and M. Gruebele, J. Chem. Phys. **141**, 035103 (2014).
[10] G. Loget and A. Kuhn, Nat. Commun. **2**, 535 (2011).
[11] N. Elsner, C. P. Royall, B. Vincent, and D. R. E. Snoswell, J. Chem. Phys. **130**, 154901 (2009).
[12] S. Jäger and S. H. L. Klapp, Soft Matter **7**, 6606 (2011).
[13] A. Prokop, J. Vacek, and J. Michl, ACS Nano **6**, 1901 (2012).
[14] F. Ma, D. T. Wu, and N. Wu, J. Am. Chem. Soc. **135**, 7839 (2013).
[15] T. Uzer, C. Jaffé, J. Palacián, P. Yanguas, and S. Wiggins, Nonlinearity **15**, 957 (2002).
[16] Z. C. Kramer, B. K. Carpenter, G. S. Ezra, and S. Wiggins, J. Phys. Chem. A **119**, 6611 (2015).
[17] T. Komatsuzaki and R. S. Berry, Proc. Natl. Acad. Sci. USA **98**, 7666 (2001).
[18] H. Teramoto, G. Haller, and T. Komatsuzaki, Chaos **23**, 043107 (2013).
[19] U. Çiftçi and H. Waalkens, Phys. Rev. Lett. **110**, 233201 (2013).
[20] D. G. Truhlar and B. C. Garrett, Annu. Rev. Phys. Chem. **35**, 159 (1984).
[21] R. Hernandez and W. H. Miller, Chem. Phys. Lett. **214**, 129 (1993).
[22] W. H. Miller, Acc. Chem. Res. **26**, 174 (1993).
[23] D. G. Truhlar, B. C. Garrett, and S. J. Klippenstein, J. Phys. Chem. **100**, 12771 (1996).
[24] H. Waalkens, R. Schubert, and S. Wiggins, Nonlinearity **21**, R1 (2008).
[25] T. Bartsch, J. M. Moix, R. Hernandez, S. Kawai, and T. Uzer, Adv. Chem. Phys. **140**, 191 (2008).
[26] S. Kawai and T. Komatsuzaki, Phys. Rev. Lett. **105**, 048304 (2010).
[27] R. Hernandez, T. Bartsch, and T. Uzer, Chem. Phys. **370**, 270 (2010).
[28] O. Sharia and G. Henkelman, New J. Phys. **18**, 013023 (2016).
[29] R. G. Mullen, J.-E. Shea, and B. Peters, J. Chem. Phys. **140**, 041104 (2014).
[30] A. M. Ozorio de Almeida, N. de Leon, M. A. Mehta, and C. C. Marston, Physica D (Amsterdam) **46**, 265 (1990).
[31] N. De Leon, M. A. Mehta, and R. Q. Topper, J. Chem. Phys. **94**, 8310 (1991).
[32] C.-B. Li, A. Shoujiguchi, M. Toda, and T. Komatsuzaki, Phys. Rev. Lett. **97**, 028302 (2006).
[33] G. S. Ezra, H. Waalkens, and S. Wiggins, J. Chem. Phys. **130**, 164118 (2009).
[34] G. S. Ezra and S. Wiggins, J. Phys. A **42**, 205101 (2009).
[35] H. Teramoto, M. Toda, and T. Komatsuzaki, Phys. Rev. Lett. **106**, 054101 (2011).
[36] H. Waalkens and S. Wiggins, J. Phys. A **37**, L435 (2004).
[37] M. Iñarrea, J. F. Palacián, A. I. Pascual, and J. P. Salas, J. Chem. Phys. **135**, 014110 (2011).
[38] A. Allahem and T. Bartsch, J. Chem. Phys. **137**, 214310 (2012).
[39] R. S. MacKay and D. C. Strub, Nonlinearity **27**, 859 (2014).
[40] H. Teramoto, M. Toda, M. Takahashi, H. Kono, and T. Komatsuzaki, Phys. Rev. Lett. **115**, 093003 (2015).
[41] T. Bartsch, R. Hernandez, and T. Uzer, Phys. Rev. Lett. **95**, 058301 (2005).
[42] T. Bartsch, T. Uzer, and R. Hernandez, J. Chem. Phys. **123**, 204102 (2005).
[43] T. Bartsch, T. Uzer, J. M. Moix, and R. Hernandez, J. Chem. Phys. **124**, 244310 (2006).
[44] T. Bartsch, T. Uzer, J. M. Moix, and R. Hernandez, J. Phys. Chem. B **112**, 206 (2008).
[45] K. Yamanouchi, Science **295**, 1659 (2002).
[46] B. J. Sussman, D. Townsend, M. Y. Ivanov, and A. Stolow, Science **314**, 278 (2006).
[47] S. Kawai and T. Komatsuzaki, J. Chem. Phys. **134**, 024317 (2011).
[48] A. Sethi and S. Keshavamurthy, Phys. Rev. A **79**, 033416 (2009).
[49] S. Patra and S. Keshavamurthy, Chem. Phys. Lett. **634**, 1 (2015).
[50] F. Revuelta, R. Chacón, and F. Borondo, Europhys. Lett. **110**, 40007 (2015).
[51] R. Q. Topper, Rev. Comput. Chem. **10**, 101 (1997).
[52] B. K. Carpenter, Annu. Rev. Phys. Chem. **56**, 57 (2005).
[53] P. Collins, B. K. Carpenter, G. S. Ezra, and S. Wiggins, J. Chem. Phys. **139**, 154108 (2013).
[54] P. Collins, Z. C. Kramer, B. K. Carpenter, G. S. Ezra, and S. Wiggins, J. Chem. Phys. **141**, 034111 (2014).

[55] S. W. Flynn, H. C. Zhao, and J. R. Green, J. Chem. Phys. **141**, 104107 (2014).
[56] J. W. Nichols, S. W. Flynn, and J. R. Green, J. Chem. Phys. **142**, 064113 (2015).
[57] G. T. Craven, T. Bartsch, and R. Hernandez, J. Chem. Phys. **141**, 041106 (2014).
[58] G. T. Craven, T. Bartsch, and R. Hernandez, J. Chem. Phys. **142**, 074108 (2015).
[59] G. T. Craven, T. Bartsch, and R. Hernandez, Phys. Rev. E **89**, 040801 (2014).
[60] F. Revuelta, G. T. Craven, T. Bartsch, F. Borondo, R. M. Benito, and R. Hernandez J. Chem. Phys. **147**, 074104 (2017).
[61] S. Kawai, A. D. Bandrauk, C. Jaffé, T. Bartsch, J. Palacián, and T. Uzer, J. Chem. Phys. **126**, 164306 (2007).
[62] D. Blazevski and R. de la Llave, J. Phys. A **44**, 195101 (2011).
[63] D. Blazevski and J. Franklin, Chaos **22**, 043138 (2012).
[64] M. Canadell and R. de la Llave, Physica D (Amsterdam) **310**, 104 (2015).
[65] F. Revuelta, T. Bartsch, R. M. Benito, and F. Borondo, J. Chem. Phys. **136**, 091102 (2012).
[66] T. Bartsch, F. Revuelta, R. M. Benito, and F. Borondo, J. Chem. Phys. **136**, 224510 (2012).
[67] C. Mendoza and A. M. Mancho, Phys. Rev. Lett. **105**, 038501 (2010).
[68] A. M. Mancho, S. Wiggins, J. Curbelo, and C. Mendoza, Commun. Nonlinear Sci. Numer. Simul. **18**, 3530 (2013).
[69] G. T. Craven and R. Hernandez, Phys. Rev. Lett. **115**, 148301 (2015).
[70] A. Junginger and R. Hernandez, J. Phys. Chem. B **120**, 1720 (2016).
[71] G. T. Craven and R. Hernandez, Phys. Chem. Chem. Phys. **18**, 4008 (2016).
[72] R. Zwanzig, *Nonequilibrium Statistical Mechanics* (Oxford University Press, London, 2001).
[73] A. Junginger, G. T. Craven, T. Bartsch, F. Revuelta, F. Borondo, R. M. Benito, and R. Hernandez, Phys. Chem. Chem. Phys. **18**, 30270 (2016).
[74] A. Junginger and R. Hernandez, Phys. Chem. Chem. Phys. **18**, 30282 (2016).
[75] F. Revuelta, T. Bartsch, P. L. Garcia-Muller, R. Hernandez, R. M. Benito, and F. Borondo, Phys. Rev. E **93**, 062304 (2016).
[76] M. Feldmaier, A. Junginger, J. Main, G. Wunner, and R. Hernandez, arXiv:1705.00248.
[77] S. Balasuriya and K. Padberg-Gehle, Phys. Rev. E **90**, 032903 (2014).
[78] A. Shukla and S. Keshavamurthy, J. Phys. Chem. B **119**, 11326 (2015).
[79] S. Torquato, *Random Heterogenous Materials: Microstructure and Macroscopic Properties* (Springer-Verlag, New York, 2002).
[80] G. T. Craven, A. V. Popov, and R. Hernandez, J. Chem. Phys. **138**, 244901 (2013).
[81] G. T. Craven, A. V. Popov, and R. Hernandez, Soft Matter **10**, 5350 (2014).
[82] G. T. Craven, A. V. Popov, and R. Hernandez, J. Chem. Phys. **142**, 154906 (2015).
[83] D. Coslovich and A. Ikeda, Soft Matter **9**, 6786 (2013).
[84] N. B. Wilding and P. Sollich, J. Chem. Phys. **141**, 094903 (2014).
[85] S. Prestipino and F. Saija, J. Chem. Phys. **141**, 184502 (2014).